



LAWRENCE  
LIVERMORE  
NATIONAL  
LABORATORY

# Statistical Measurements of Scaling and Anisotropy of Turbulent Flows Induced by Rayleigh-Taylor Instability

W. H. Cabot, Y. Zhou

September 28, 2012

Physics of Fluids

## **Disclaimer**

---

This document was prepared as an account of work sponsored by an agency of the United States government. Neither the United States government nor Lawrence Livermore National Security, LLC, nor any of their employees makes any warranty, expressed or implied, or assumes any legal liability or responsibility for the accuracy, completeness, or usefulness of any information, apparatus, product, or process disclosed, or represents that its use would not infringe privately owned rights. Reference herein to any specific commercial product, process, or service by trade name, trademark, manufacturer, or otherwise does not necessarily constitute or imply its endorsement, recommendation, or favoring by the United States government or Lawrence Livermore National Security, LLC. The views and opinions of authors expressed herein do not necessarily state or reflect those of the United States government or Lawrence Livermore National Security, LLC, and shall not be used for advertising or product endorsement purposes.

## **Statistical Measurements of Scaling and Anisotropy of Turbulent Flows Induced by Rayleigh-Taylor Instability**

W. Cabot<sup>1</sup> and Ye Zhou<sup>1</sup>

*Lawrence Livermore National Laboratory, 7000 East Avenue,  
Livermore CA 94550*

(Dated: 3 December 2012)

This work investigates several key statistical measurements of turbulence induced by Rayleigh-Taylor instability using data from well resolved numerical simulations at moderate Reynolds number with the goal of determining the degree of departure of this inhomogeneous flow from that of homogeneous, isotropic turbulence. The simulations use two miscible fluids with unity Schmidt number and moderate density contrast ( $3/2$  to  $9$ ). The results of this study should find application in subgrid-scale modeling for large-eddy simulations and Reynolds-Averaged Navier-Stokes modeling used in many engineering and scientific problems.

PACS numbers: 47.27.ek, 47.20.Ma, 47.27.wj, 47.27.eb, 47.27.Jv, 47.27.E-

Keywords: Rayleigh-Taylor instability, turbulence theory, turbulence simulation

## I. INTRODUCTION

There is considerable interest in the turbulent flows induced by Rayleigh-Taylor instability (RTI)<sup>1,2</sup> in both engineering and scientific applications. Briefly, RTI is initiated when a heavier layer of fluid is placed on the top of a layer of lighter fluid in a gravitational field. Small perturbations at the interface make it unstable and, as a result, lead to the further growth of the instability and the release of gravitational potential energy. Visualization of RTI-induced flow in its linear and nonlinear stages shows that the heavier fluid moves down in a shape of fingers or mushrooms. When the density difference between the heavy and light fluids is small, the displaced light fluids move up with a similar shape. This near symmetry breaks down when the density disparity increases. The Atwood number

$$A = \frac{\rho_2 - \rho_1}{\rho_2 + \rho_1} . \quad (1)$$

is used to characterize this disparity, where  $\rho_1$  and  $\rho_2$  are the constant values of density for light and heavy fluids in their pure, unmixed state.

It is of considerable interest to compare and contrast statistics from RTI-induced turbulent flow, which is inhomogeneous in the vertical direction as a direct result of the external driving force along the direction of the gravity or acceleration, with statistics from homogeneous, isotropic turbulence (HIT). The buoyancy production induced by gravity acts predominantly at low wave numbers (long wavelengths), and as a result, it can be viewed as an analogue of forcing functions that have been employed extensively in fully resolved direct numerical simulations (DNS) of forced HIT. The main challenge is to determine in turbulent RTI-induced flow the degree of departure from isotropy and the appropriate scaling laws in directions both aligned with and perpendicular to gravity. The goal of this paper is to present many of these key measurements calculated from well resolved direct numerical simulations of turbulent miscible fluids<sup>5</sup>. The information obtained will be very useful for future modeling efforts using large-eddy simulation (LES) and Reynolds-averaged Navier-Stokes (RANS) approaches.

## II. NUMERICAL SIMULATIONS

Direct numerical simulations of RTI flow were performed using the variable-density Navier-Stokes equations for incompressible flow without surface tension in the conservative

form:

$$(\rho Y_\alpha)_{,t} + (\rho Y_\alpha u_j)_{,j} = (\rho D Y_{\alpha,j})_{,j} ; \quad (2)$$

$$(\rho u_i)_{,t} + (\rho u_i u_j)_{,j} = \rho g_i - p_{,i} + \tau_{ij,j} . \quad (3)$$

Here  $u_i$  is the mass-averaged velocity component in direction  $x_i$ ,  $\rho$  is the mass density,  $p$  is the pressure,  $D$  is the Fickian diffusivity,  $Y_\alpha$  is the mass fraction of species  $\alpha = 1$  or  $2$ , and  $g_i$  is the acceleration defined as  $(0, 0, -g)$ . The stress tensor  $\tau_{ij}$  is given by

$$\tau_{ij} = 2\mu S_{ij}^* , \quad S_{ij}^* = S_{ij} - \frac{\delta_{ij}}{3} S_{kk} , \quad S_{ij} = \frac{1}{2} (u_{i,j} + u_{j,i}) , \quad (4)$$

where  $\mu$  is the dynamical viscosity. We use the convention of summation over repeated Roman indices, but no summation over repeated Greek indices. The spatial coordinates  $x_i$  are also designated as  $(x, y, z)$  and the velocity components  $u_i$  as  $(u, v, w)$ . Spatial indices 1 & 2 refer to the homogeneous horizontal directions and 3 refers to the vertical direction aligned with gravity. Summing Eq. (2) over species  $\alpha$  yields the familiar continuity equation. In incompressible flow, values of pure-fluid density  $\rho_\alpha$  are constant, and variations in density  $\rho$  arise solely in mixtures. The mass fraction  $Y_1 = 1 - Y_2$  is related to the density by

$$Y_1 = (\rho^{-1} - \rho_2^{-1}) / (\rho_1^{-1} - \rho_2^{-1}) . \quad (5)$$

With Eq. (2), the incompressibility condition on the dilatation (velocity divergence) is

$$\nabla \cdot \mathbf{u} = \nabla \cdot \rho D \nabla \rho^{-1} . \quad (6)$$

Unlike incompressible flow, this generally gives rise to a finite dilatation, but, even so, it is found to be negligibly small in the late-time, fully developed turbulent state. Both diffusivity  $D$  and the kinematical viscosity  $\nu = \mu/\rho$  are set to the same constant value to give a Schmidt number  $Sc = \nu/D = 1$ . Details of the numerical scheme are given by Cook et al. (2004)<sup>3</sup> and Jang & de Bruyn Kops (2007)<sup>4</sup>, and a description of a large DNS with Atwood number  $A=0.5$  is given by Cabot & Cook (2006)<sup>5</sup> with additional results presented by Cabot (2006)<sup>6</sup>. For low Atwood number ( $A \leq 0.5$ ) the simulations used 10th-order compact spatial derivatives and 3rd-order Adams-Bashford-Moulton time advancement with a fairly sharp low-pass filter to suppress aliasing errors. A 3rd-order extrapolation of the density time derivative allows the variable-density incompressibility condition in Eq. (6) to be satisfied with a single-pass solution of a Poisson equation for the pressure. For higher Atwood numbers, an alternative

4th-order Runge-Kutta time advancement scheme<sup>7</sup> was used, and multiple iterations were made on the pressure field to satisfy (6), both of which were found to improve numerical accuracy and stability.

Runs were performed in approximately cubic numerical domains with uniform grid spacing. Free-slip impermeable boundaries were imposed at the top and bottom of the domain, and periodic boundaries were imposed in the two horizontal directions. The flows were initialized with a stationary interface between the high and low density fluids whose vertical position was perturbed with random variations having a characteristic horizontal wavelength  $\lambda_0$ , which act to seed the instability; the simulations proceeded until the mixing layer filled 60–70% of the domain in the vertical direction. The  $A = 0.5$  ( $\rho_2/\rho_1 = 3$ ) case used  $3072^3$  grid points<sup>5</sup>, while the  $A = 0.2$  ( $\rho_2/\rho_1 = 3/2$ ) simulation used only  $2048^3$  grid points and the  $A = 0.8$  ( $\rho_2/\rho_1 = 9$ ) simulation used  $2048^2 \times 2304$  grid points.

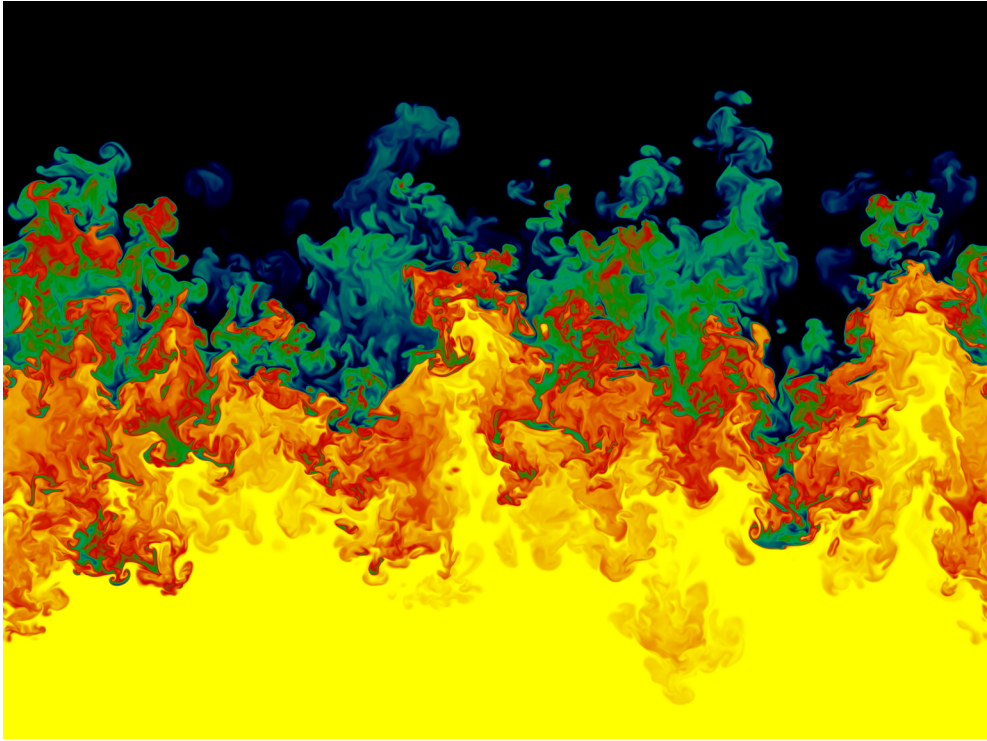


FIG. 1. (Color online) Visualization of a vertical slice of the density field in the RTI mixing layer at late time for the  $A = 0.5$  case<sup>5</sup>. Heavy fluid is dark, light fluid is light. Gravity is directed downwards.

A visualization of the turbulent mixing layer in RTI-induced flow at late time is shown in Figure 1 from the simulation for  $A = 0.5$ . Flow induced by RTI experiences several stages of

growth. Small perturbation modes at first develop in the linear regime largely independent of each other. The growth eventually enters a nonlinear, coupled regime, developing chaotic structure. If allowed to develop long enough, the flow becomes fully turbulent in the final stage, characterized by large Reynolds numbers (defined as a length scale times velocity scale divided by viscosity) and self-similar behavior. For the range of moderate density ratios considered here ( $A = 0.2$ – $0.8$ ), the flow displays little visual asymmetry. Near the end of the simulations, the largest structures in the flow may begin to be affected by the finite numerical domain, so we choose a time somewhat before this but late enough so that the turbulence is fairly well developed. Note that even at late times in the simulations the global production and dissipation rates have still not completely reached a steady self-similar state<sup>5,6</sup>, and examination of the turbulent statistics in the next section casts some doubt on whether these flows have attained a fully turbulent, high Reynolds number state.

*In the statistics presented hereafter, lengths are scaled by initial perturbation wavelength  $\lambda_0$  and times are scaled by  $(\lambda_0/gA)^{1/2}$ , unless otherwise noted.* (Note that the value of  $\lambda_0$  loses all meaning once the flow develops well into the turbulent regime; it is merely used as a fiducial with respect to the initial state.) Most of the statistics presented here are from the  $A = 0.5$  case, which is the largest simulation and provides the best statistics. Typically we will show results at a scaled time  $t = 25$  late in the simulations, at which time *small-scale motions* in the flow are approaching isotropy as measured by the ratio of vertical to horizontal enstrophy (vorticity squared) components in the middle of the mixing layer, shown in Figure 2a. The  $A = 0.8$  case lags slightly behind the lower Atwood number cases at late times, indicating that small-scale anisotropy may be more persistent for very high density ratios.

The vertical extent of the mixing region can be expressed in terms of the product width  $h$ , defined for a stoichiometric value of  $1/2$  as<sup>3</sup>

$$h = 2 \int_{-\infty}^{\infty} \min(\langle X_1 \rangle, \langle X_2 \rangle) dz , \quad (7)$$

where  $\langle X_\alpha \rangle$  is the horizontally averaged mole fraction of species  $\alpha$ . The product width is approximately one half of the full mixing layer width delineated by the 5% and 95% mean concentration levels. At late times the product width grows quadratically with time, as seen in Figure 2b. The prefactor  $\alpha$  on the modeled quadratic growth term  $\alpha g A t^2$  is similar for all Atwood numbers, falling in the range 0.020–0.024. The mixing layer width,

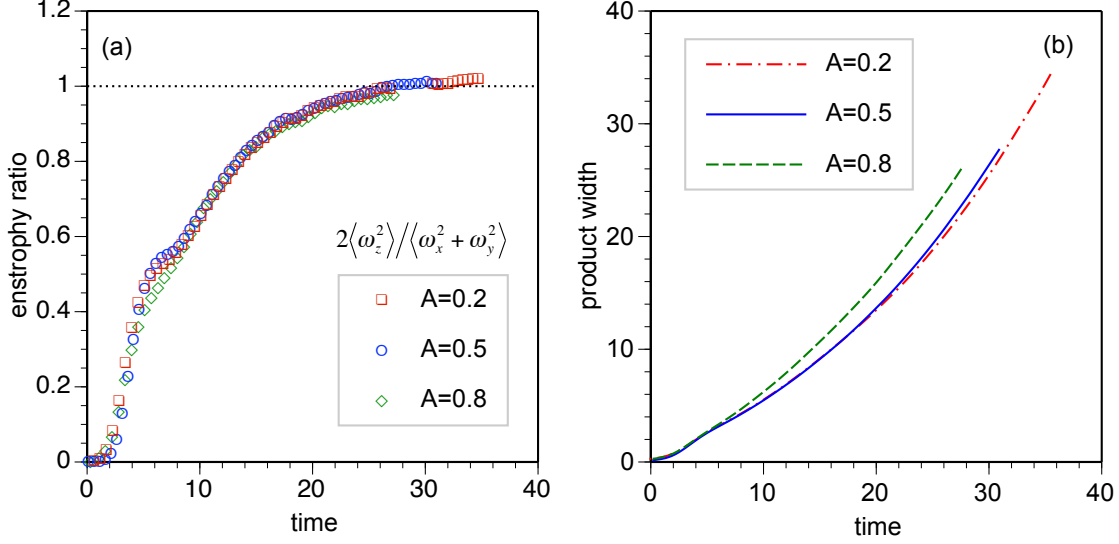


FIG. 2. (Color online) (a) Isotropy of the vorticity field is shown as a function of time, measured by the ratio of vertical to horizontal enstrophy components averaged over a vertical extent of  $h/3$  in the middle of the mixing layer. (The gap in the  $A = 0.2$  data resulted from data lost in a catastrophic file system failure.) (b) The growth of the product width  $h$  is shown for the different Atwood numbers.

whatever its definition, is often used as the large outer scale for turbulent RTI flow and its time derivative is used as a velocity scale<sup>5,6</sup>; hence an outer scale Reynolds number can be defined as  $Re_h = h\dot{h}/\nu$ , which attains values of about  $10^4$  at late times in the simulations discussed here. The Reynolds number based on the Taylor microscale is a less arbitrary metric to characterize turbulence, and it will be discussed in more detail in §III B.

### III. STATISTICAL MEASUREMENTS

#### A. Isotropy of the velocity and its derivatives

Vertical profiles of the fluctuation intensity (square of the rms) of the velocity components and their various spatial derivatives across the mixing region at late times are shown in Figure 3. The velocity components in Figure 3a display a high degree of anisotropy; the fluctuation intensity of the velocity derivatives in Figure 3b, on the other hand, tend to be much more isotropic. These properties are seen to extend across the entire mixing re-



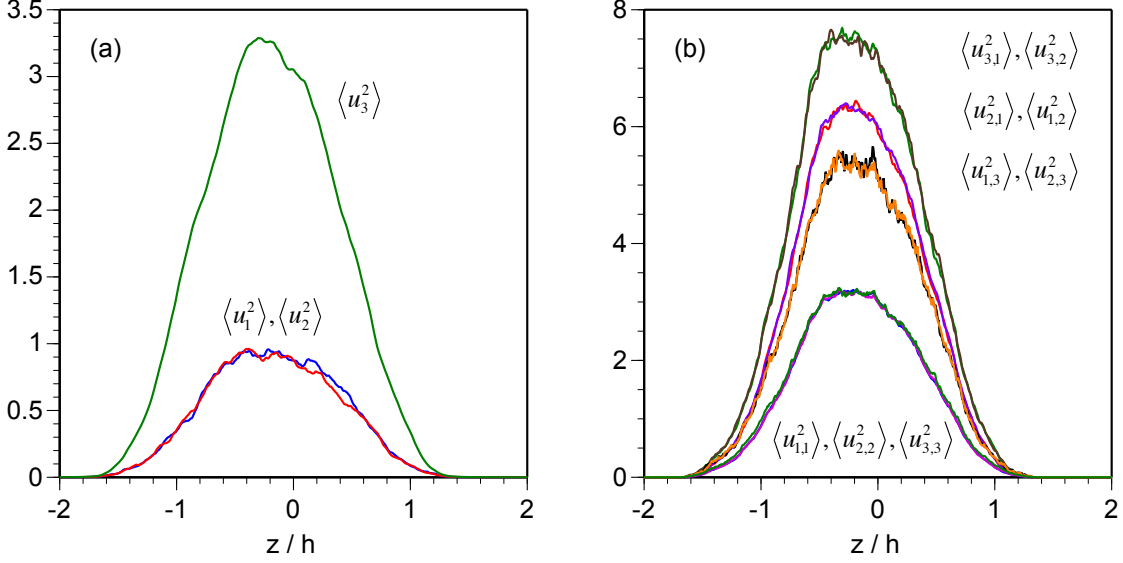


FIG. 3. (Color online) Vertical profiles (horizontal averages) of fluctuation intensity for (a) velocity components and (b) velocity derivative components are shown at time  $t = 25$  in the  $A = 0.5$  case, demonstrating statistical equivalences and the degree of anisotropy.

gion. While the statistics of velocity components in RTI flow directly reflect the anisotropic production of energy by buoyancy predominantly at larger scales, the statistics of velocity derivatives are weighted toward much smaller scales that are less directly affected by the anisotropic production. The small-scale motions become more isotropic through the turbulent cascade process, an effect that has been previously noted in RTI flow<sup>36</sup> and also observed in anisotropically forced channel and pipe flows<sup>8</sup>.

Profiles of the fluctuation intensity of the various velocity derivatives in Figure 3b show both isotropy and anisotropy with respect to homogeneous isotropic turbulence (HIT). Velocity derivatives  $u_{\alpha,\beta}$  for which  $\alpha \neq \beta$  are called “transverse”, and those with  $\alpha = \beta$  are called “longitudinal”. All of the longitudinal velocity derivatives ( $u_{\alpha,\alpha}$ ) have isotropic fluctuations, probably because the flow is nearly divergence-free, and these are half as large in intensity as those for the horizontal transverse derivatives of horizontal velocity components ( $u_{1,2}$  and  $u_{2,1}$ ), the same as found in HIT<sup>9</sup>. In HIT, all transverse derivatives would give the same fluctuation intensity. However, in RTI flow the horizontal transverse derivatives of the vertical velocity component ( $u_{3,1}$  and  $u_{3,2}$ ) are larger by about 17%, and the vertical transverse derivatives of the horizontal velocity components ( $u_{1,3}$  and  $u_{2,3}$ ) are smaller by

TABLE I. Velocity and velocity-derivative isotropy in homogeneous isotropic turbulence (theoretical) and late-time ( $t = 25$ ) Rayleigh-Taylor instability flow with gravity in direction 3.

Flow	$\langle u_3^2 \rangle / \langle u_1^2 \rangle$	$\langle u_{3,3}^2 \rangle / \langle u_{1,1}^2 \rangle$	$\langle u_{1,2}^2 \rangle / \langle u_{1,1}^2 \rangle$	$\langle u_{1,3}^2 \rangle / \langle u_{1,1}^2 \rangle$	$\langle u_{3,1}^2 \rangle / \langle u_{3,3}^2 \rangle$	$\langle u_{\alpha,\beta} u_{\beta,\alpha} \rangle / \langle u_{\beta,\beta}^2 \rangle$
HIT	1	1	2	2	2	-1/2
RTI ( $A = 0.2$ )	3.379	1.029	1.975	1.693	2.376	-0.500
RTI ( $A = 0.5$ )	3.463	1.030	1.969	1.709	2.356	-0.499
RTI ( $A = 0.8$ )	3.400	1.033	1.965	1.698	2.344	-0.497

same amount, such that their average is the same as the horizontal-horizontal transverse combination. This means that both the vertical velocity ( $u_3$ ) and the characteristic vertical length scales, measured by Taylor microscales  $(\langle u_1^2 \rangle / \langle u_{1,3}^2 \rangle)^{1/2}$  and  $(\langle u_2^2 \rangle / \langle u_{2,3}^2 \rangle)^{1/2}$ , are larger than their horizontal counterparts in RTI flow, but not in equal measure, i.e., there is greater asymmetry in the velocity components than in their derivative length scales, reflecting the greater anisotropy of the largest scales. Values of these ratios are given in Table I for HIT and late-time RTI flow; all statistics in this table are globally averaged near a scaled time of  $t = 25$ , and statistically equivalent terms have been averaged together. The rightmost column is calculated with  $\langle u_{1,2}u_{2,1} + u_{2,3}u_{3,2} + u_{3,1}u_{1,3} \rangle / \langle u_{1,1}^2 + u_{2,2}^2 + u_{3,3}^2 \rangle$ . RTI results are seen to be insensitive to the Atwood number (density contrast) over the intermediate range of values simulated.

The enstrophy components  $\langle \omega_\gamma^2 \rangle = \langle (u_{\beta,\alpha} - u_{\alpha,\beta})^2 \rangle$ , where  $\alpha \neq \beta \neq \gamma$ , are seen to approach isotropy at late time in Figs. 2a & 4a. The combinations  $\langle u_{\alpha,\beta}^2 \rangle + \langle u_{\beta,\alpha}^2 \rangle$ ,  $\alpha \neq \beta$ , have nearly isotropic values, as deduced from Figure 3b, as do the cross terms  $\langle u_{\alpha,\beta} u_{\beta,\alpha} \rangle$  shown in Figure 4b. This also implies that the off-diagonal strain terms  $\langle 4S_{\alpha\beta}^2 \rangle = \langle (u_{\alpha,\beta} + u_{\beta,\alpha})^2 \rangle$ ,  $\alpha \neq \beta$ , are also nearly isotropic, as well as the diagonal ones  $\langle S_{\alpha\alpha}^2 \rangle = \langle u_{\alpha,\alpha}^2 \rangle$ . We can define the mass-specific dissipation rate associated with each velocity component as

$$\langle \varepsilon_\alpha \rangle = \langle 2\nu u_{\alpha,i} S_{\alpha i}^* \rangle, \quad (8)$$

which comprise different mixtures of velocity derivative terms and remain anisotropic (see Fig. 4c), with the vertical direction about 20% larger than those for the horizontal directions for the  $A=0.5$  case. The usual relation in HIT that  $\langle \varepsilon_\alpha \rangle = \nu \langle \omega_\alpha^2 \rangle$  for any  $\alpha$  does not hold in RTI flow; instead it is straightforward to show, using Table I and assuming negligible

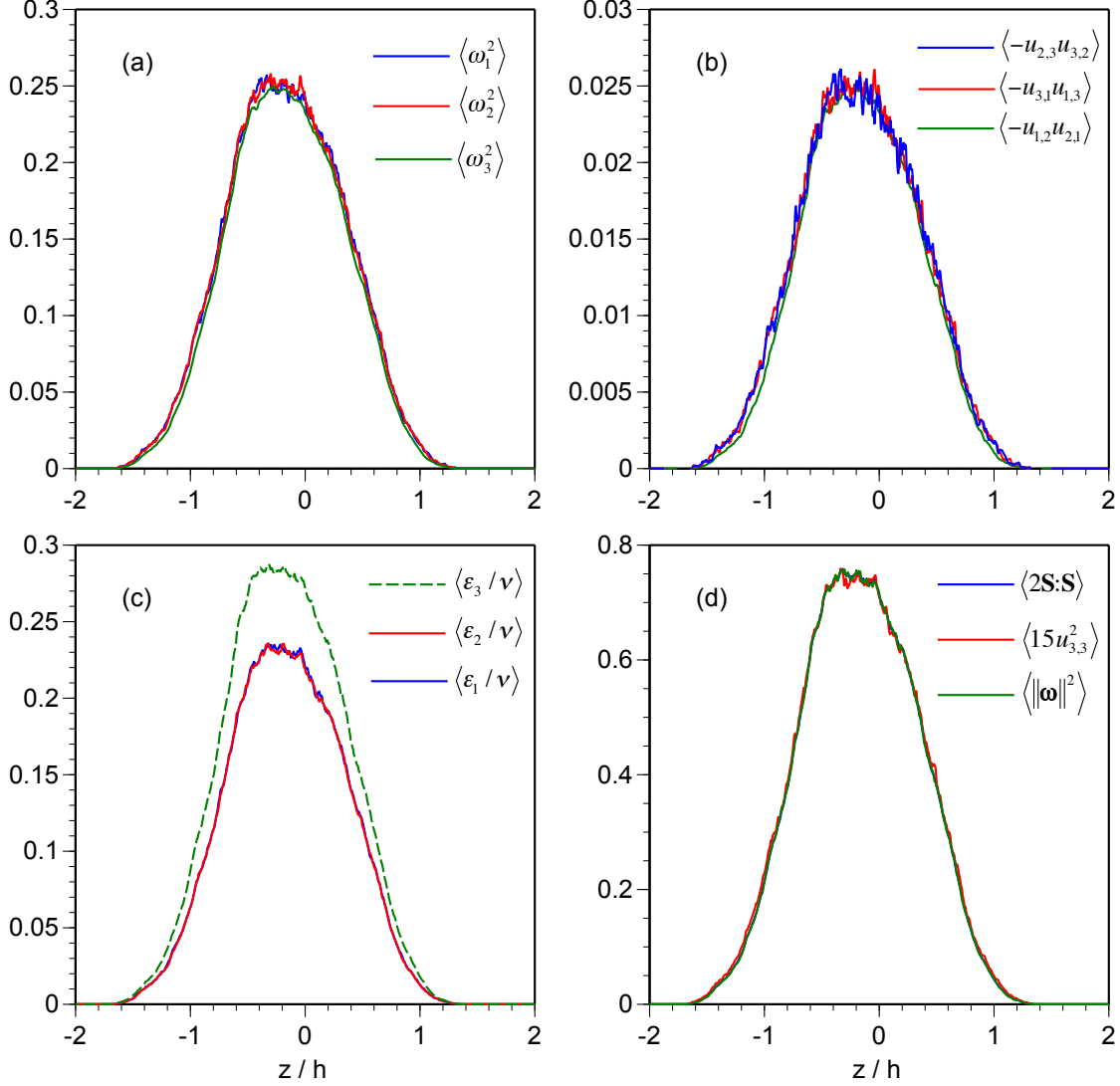


FIG. 4. (Color online) Vertical profiles (horizontal averages) of the fluctuation intensity of velocity derivative functions at time  $t = 25$  in the  $A = 0.5$  case: (a) vorticity components, (b) cross terms, (c) dissipation components, and (d) dissipation terms. The vertical position is scaled by the product width of the mixing layer  $h$ .

dilatation, that

$$\langle \varepsilon_3 \rangle \approx \nu \langle \omega_2^2 \rangle + \nu \langle u_{3,1}^2 - u_{1,3}^2 \rangle, \quad \langle \varepsilon_1 \rangle \approx \langle \varepsilon_2 \rangle \approx \nu \langle \omega_2^2 \rangle - \frac{\nu}{2} \langle u_{3,1}^2 - u_{1,3}^2 \rangle, \quad (9)$$

where  $\langle u_{1,3}^2 \rangle \approx 0.72 \langle u_{3,1}^2 \rangle$ . This anisotropy is needed to balance the larger rate of production that the vertical velocity experiences directly through buoyancy and which has not been equitably distributed to the other components through the pressure-strain terms. Despite

the anisotropy in individual dissipation components, the total dissipation rate in the middle of the mixing layer at late times is still found to satisfy the homogeneous relations

$$\langle \varepsilon \rangle = \sum_{j=1}^3 \langle \varepsilon_j \rangle = 2\nu \langle S_{ij}^* S_{ij}^* \rangle \approx \nu \langle \omega_i \omega_i \rangle \approx 15\nu \langle u_{\alpha,\alpha}^2 \rangle \quad (10)$$

for any  $\alpha$ , as seen in Figure 4d. The cross-term averages also satisfy the homogeneous relations

$$\langle -u_{\alpha,\beta} u_{\beta,\alpha} \rangle \approx \frac{1}{2} \langle u_{\gamma,\gamma}^2 \rangle \approx \frac{1}{10} \langle \omega_\gamma^2 \rangle \quad (11)$$

for any combination with  $\alpha \neq \beta$  and any  $\gamma$ . Thus the statistics of many combinations of velocity derivative fluctuations become surprisingly isotropic while others retain the imprint of the large-scale anisotropy found in the velocity components themselves (see Table I).

## B. Length scales

The initial interface perturbations in the  $A = 0.5$  simulation had a well resolved dominant wavelength of  $\lambda_0 = 32$  grid points. The initial interface perturbations for the other Atwood number cases were slightly less well resolved, with  $\lambda_0 = 16$  grid points for  $A = 0.2$  and  $\lambda_0 = 21$  grid points for  $A = 0.8$ . The product widths of the mixing layer  $h$  are  $\sim 20$  in units of  $\lambda_0$  at  $t = 25$  and  $\sim 30$  near the end of the runs (see Fig. 2b). The definitions of turbulence length scales are typically anisotropic and will depend on the location of spatial averaging due to variations in the vertical direction. The Taylor microscale can be defined per velocity component and direction as

$$\lambda_{\alpha,\beta} = \left( \langle u_\alpha^2 \rangle / \langle u_{\alpha,\beta}^2 \rangle \right)^{1/2}, \quad (12)$$

where it is understood that fluctuating parts of the velocity components are used and angle brackets represent a spatial average. Typically longitudinal derivatives are considered ( $\alpha = \beta$ ). As in isotropic turbulence, the total mean mass-specific dissipation rate is  $\langle \varepsilon \rangle \approx 15\nu \langle u_{\alpha,\alpha}^2 \rangle$ , so the longitudinal component Taylor microscale can be approximated by

$$\lambda_{\alpha,\alpha} \approx \left( 15\nu \langle u_\alpha^2 \rangle / \langle \varepsilon \rangle \right)^{1/2}, \quad (13)$$

which scales as  $\langle u_\alpha^2 \rangle^{1/2}$ . A component Taylor microscale Reynolds number is then given by

$$Re_{\lambda_\alpha} = \langle u_\alpha^2 \rangle^{1/2} \lambda_{\alpha,\alpha} / \nu, \quad (14)$$

TABLE II. Turbulence statistics for the  $A = 0.5$  case at  $t = 25$  for different spatial averaging domains.

average	$\langle u_1^2 \rangle$	$\langle u_3^2 \rangle$	$\langle u_{1,1}^2 \rangle$	$\langle u_{3,3}^2 \rangle$	$\langle \varepsilon_1 \rangle$	$\langle \varepsilon_3 \rangle$	$\eta$	$\lambda_{1,1}$	$\lambda_{3,3}$	$Re_{\lambda 1}$	$Re_{\lambda 3}$
midplane	0.875	3.051	3.007	3.030	0.110	0.136	0.0340	0.539	1.003	65	224
mid-slab	0.873	3.037	2.966	2.985	0.109	0.134	0.0341	0.543	1.009	65	225
global								0.572	1.041		

which scales as  $\langle u_\alpha^2 \rangle$ ; hence the vertical value will be 3–4 times the horizontal one (see Tables I–III). The Kolmogorov dissipation scale is usually given in its isotropic form as

$$\eta = (\nu^3 / \langle \varepsilon \rangle)^{1/4}, \quad (15)$$

although one could instead use 3 times the dissipation rate for each component  $\langle \varepsilon_\alpha \rangle$  given in (8). At late times the vertical dissipation rate is about 20% larger than the horizontal, giving only a 5% difference in  $\eta_\alpha$  values, so we will only report the isotropic value of  $\eta$  here. The spatial averaging domain (denoted by angle brackets) can be (1) a plane such as the midplane, (2) a volume enclosing fairly homogeneous turbulence with vertical extent considerably narrower than the width of the mixing layer, e.g., a slab centered on the midplane, or (3) the entire numerical domain for a global average. Global averages must be normalized with a representative height scale to account for the vertical inhomogeneity, which is rather arbitrary; we therefore only report global values of  $\lambda_{\alpha,\alpha}$ , which are unambiguous ratios of global averages. Table II gives the values of these quantities in scale units using different averaging domains for the  $A = 0.5$  case with  $\nu = 1/128$  in scaled units. Both horizontal directions are averaged together in these results. The “mid-slab” domain uses an unweighted average of data spanning a vertical extent of  $h/3$  centered on the midplane, and it gives values in close agreement with the midplane averages. The same “mid-slab” statistics are given in Table III for different values of Atwood number near the end of each simulation when Reynolds numbers attain their greatest values ( $\nu$  in scaled units is  $\sqrt{5}/256 \approx 1/114$  for  $A = 0.2$  and  $\sqrt{135}/1024 \approx 1/88$  for  $A = 0.8$ ); these show the same trends as in Table II.

There is a fair degree of separation between the longest, intermediate, and smallest physical length scales at late times in the numerical simulation results with  $h : \lambda : \eta \approx 20 : 1 : 1/30$ . In HIT<sup>12</sup>, the largest scale is represented by an “inertial scale” or “outer scale”  $\ell = K^{3/2}/\varepsilon$ , where  $K$  is the kinetic energy of turbulent motions, the smallest scale is rep-

TABLE III. Late-time turbulence statistics for different Atwood numbers with “mid-slab” average.

$A$	time	$\langle u_1^2 \rangle$	$\langle u_3^2 \rangle$	$\langle u_{1,1}^2 \rangle$	$\langle u_{3,3}^2 \rangle$	$\langle \varepsilon_1 \rangle$	$\langle \varepsilon_3 \rangle$	$\eta$	$\lambda_{1,1}$	$\lambda_{3,3}$	$Re_{\lambda 1}$	$Re_{\lambda 3}$
0.2	35.2	1.477	5.565	3.168	3.091	0.132	0.150	0.0356	0.683	1.342	95	362
0.5	30.5	1.257	4.403	3.402	3.360	0.126	0.147	0.0331	0.608	1.145	87	307
0.8	27.5	1.434	4.473	3.298	3.342	0.177	0.211	0.0401	0.659	1.157	70	216

resented by the Kolmogorov scale  $\eta = (\nu^3/\varepsilon)^{1/4}$ , and the intermediate scale is the Taylor microscale given by  $\lambda = (10K\nu/\varepsilon)^{1/2}$ , hence the scales are related by  $\lambda = 10^{1/2}\ell^{1/3}\eta^{2/3}$ ; if one associates  $h$  with  $\ell$ , this relation is roughly satisfied by the RTI results. Note that for very large dynamic ranges (measured by  $\ell/\eta$ ),  $\lambda$  is biased toward the smaller dissipation scales. This level of separation in scales, while satisfying from a numerical simulation standpoint, is not equivalent to the existence of an extensive inertial range and an adequate amount of separation between large, energy-containing scales and dissipation scales that is expected in fully developed turbulence. Analyses of turbulent flow spectra<sup>10,11</sup> show that the Taylor-microscale Reynolds number must be substantially greater than 100 in order for an inertial range to develop. In the numerical simulations discussed here, the Taylor-microscale Reynolds numbers for vertical velocity components are roughly 200–400 at the latest times, which may marginally qualify as fully developed turbulence, but the horizontal counterparts are considerably lower with values below 100, which clearly does not. This disparity in vertical and horizontal Reynolds numbers is also evident in the power spectra for individual velocity components shown in Figure 7 below; the requirements for the development of a true inertial range are discussed in greater detail in §III E.

### C. Correlation functions

The inhomogeneous vertical direction causes some challenge in spectral analysis of RTI-induced turbulent flows. In order to obtain the information unavailable to the spectral analysis, we turn our attention to the correlation function. When discussing correlations and spectra in one dimension, just as with the velocity derivatives, “longitudinal” refers to correlations in the same direction as the velocity component, and “transverse” refers to cor-

relations in a direction normal to the velocity component. (This nomenclature is not meaningful for density variations.) The correlation tensor is given by  $R_{ab}(\mathbf{r}) = \langle a(\mathbf{x})b(\mathbf{x} + \mathbf{r}) \rangle$ , where  $a, b$  here can be velocity components or the density, and where  $\mathbf{r}$  is the separation vector in any direction; because of inhomogeneity in the vertical direction,  $R_{ab}$  may also be height-dependent, depending on the spatial averaging domain. We choose separations along the cartesian axes, i.e.,  $\mathbf{r} = (\delta x, 0, 0)$ ,  $(0, \delta y, 0)$ , or  $(0, 0, \delta z)$ . The corresponding normalized correlation function is defined as  $C_{ab}(\mathbf{r}) = R_{ab}(\mathbf{r})/R_{ab}(0)$ . Note that  $\rho$  and  $w$  are strongly anticorrelated with  $\langle \rho w \rangle / (\rho_{rms} w_{rms}) = -0.7$  to  $-0.8$  in well developed RTI flow<sup>3</sup>.

The correlation functions for the horizontal velocity components in the middle of the mixing region are shown in Figure 5a. These horizontal correlations are averaged over a central slab with vertical range spanning  $h/3$  centered on the midplane  $z_0$ , i.e.,

$$R_{ab}(\delta x|z_0) = \frac{3}{h} \int_{z_0-h/6}^{z_0+h/6} \langle a(x, y, z)b(x + \delta x, y, z) \rangle dz . \quad (16)$$

where the angle brackets here denote an average over  $xy$  planes, and likewise for separations in the  $y$  direction. These correlations are exactly symmetric about zero separation because of the imposed periodicity. Averages over  $xy$  planes of data displaced from the midplane are used to obtain correlations in the vertical direction:

$$R_{ab}(\delta z|z_0) = \langle a(x, y, z_0)b(x, y, z_0 + \delta z) \rangle ; \quad (17)$$

these correlations are not symmetric about the midplane, as clearly seen in Figure 5a & c (solid lines), although the degree of asymmetry is fairly modest. In most turbulent flows the longitudinal correlations stay positive at all separations and transverse correlations become negative at some finite separation<sup>9,12</sup>. However, Figure 5a shows that it is the longitudinal correlations that go negative and the transverse ones that stay positive for horizontal separations of the horizontal velocity components in RTI, which may arise from the flow structure induced by the vertical forcing. The transverse vertical correlations show the normal dip into negative territory. In HIT the longitudinal correlation lengths are typically  $\sqrt{2}$  times larger than the transverse ones, and this is also observed in the widths of the correlation function profiles at small separations.

The correlation functions for the vertical velocity component  $w$  and the density  $\rho$  are shown in Figure 5b for horizontal separations using Eq. (16) and in Figure 5c for vertical separations using Eq. (17). The values of  $C_{ww}$  and  $C_{\rho w}$  are very close in both vertical and

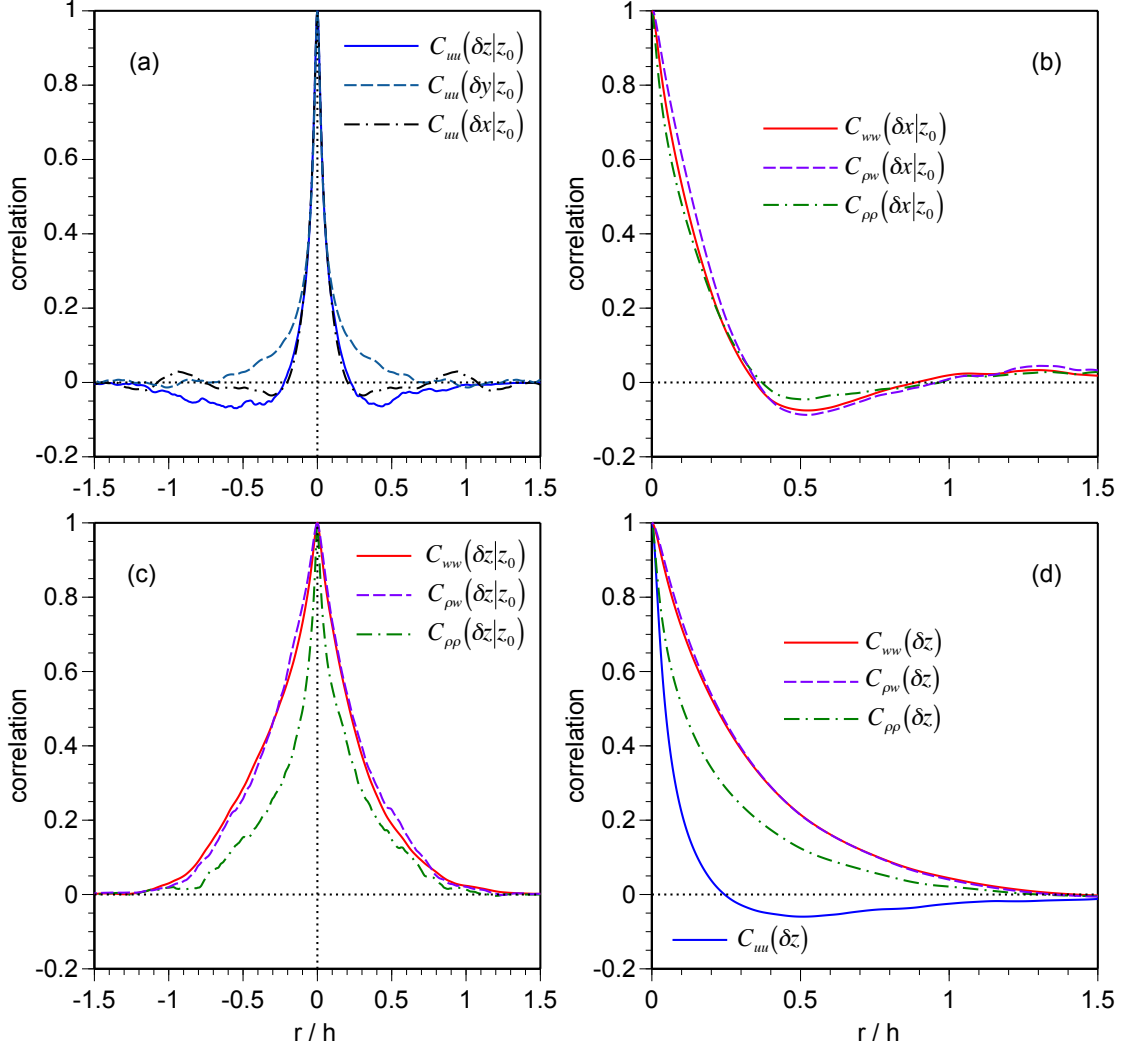


FIG. 5. (Color online) The correlation functions of velocity components and density for the  $A = 0.5$  case at  $t = 25$  using mid-slab averaging for horizontal correlations in (a) and (b), midplane averaging for vertical correlations in (a) and (c), and global vertical correlations in (d). The longitudinal horizontal correlation  $C_{uu}(\delta x|z_0)$  in (a) is plotted with the separation length scaled by  $1/\sqrt{2}$ . Statistically equivalent terms have been averaged together.

horizontal directions because of the high degree of correlation between  $\rho$  and  $w$  induced by buoyancy. These functions are much narrower in the horizontal directions than those in the vertical direction, and the former become negative with peaks at  $r/h = 0.5$ . The autocorrelation function of the density  $C_{\rho\rho}$  is quite close to  $C_{ww}$  and  $C_{\rho w}$  in the horizontal directions, but this function is somewhat narrower in the vertical direction.



Vertical correlations *using global averaging*, viz.,

$$R_{ab}(\delta z) = \frac{1}{2h} \int_{-\infty}^{\infty} \langle a(x, y, z) b(x, y, z + \delta z) \rangle dz, \quad (18)$$

are shown in Figure 5d; these are symmetric with respect to direction of separation for auto-correlations and are made symmetric for cross-correlations using  $(R_{ab} + R_{ba})/2$  combinations. The autocorrelation of the vertical velocity (longitudinal) and density fluctuations are always positive, whereas the autocorrelation of the horizontal velocity components (transverse) become negative; the vertical correlation lengths for vertical velocity are much longer than for horizontal velocity, which is to be expected from the asymmetric driving in RTI flow. The autocorrelation for vertical velocity and the cross-correlation of vertical velocity and density are again nearly identical.

A correlation length  $\Lambda_{\alpha,\beta}$  can be calculated by integrating over the autocorrelation function  $C_{\alpha\alpha}(\delta x_\beta)$ . The meaning of this is problematic for correlation functions that become negative. Furthermore, the results are inaccurate for correlation functions that do not decay to zero at maximal separations, which is a problem that arises in simulations at late times when very large-scale structures become marginally correlated on a global scale, i.e., the finite numerical domain begins to constrain the flow. A more robust measure is the HWHM of the correlation function, denoted here as  $H_{\alpha,\beta}$ , which is an intermediate length scale representing the characteristic distance of *positive* correlation of variable  $\alpha$  in direction  $\beta$ . The radius of curvature of the correlation function near the origin, corresponding to structure at smaller scales, is equal to the Taylor microscale  $\lambda_{\alpha,\beta}$ . In HIT  $\lambda_{1,2}/\lambda_{1,1} = 1/\sqrt{2}$  and  $\lambda_{3,3}/\lambda_{1,1} = \lambda_{3,2}/\lambda_{1,2} = \lambda_{1,3}/\lambda_{1,2} = 1$ ; using values in Table I, RTI flow gives  $\lambda_{1,2}/\lambda_{1,1} = 0.71$  and  $\lambda_{3,3}/\lambda_{1,1} = 1.82$ ,  $\lambda_{3,2}/\lambda_{1,2} = 1.65$ ,  $\lambda_{1,3}/\lambda_{1,2} = 1.08$ , i.e., Taylor microscales are longer for vertical velocity components than for horizontal ones, and the Taylor microscales are more isotropic for horizontal velocity components. The ratios for the HWHM correlations in RTI flow near midplane are  $H_{1,2}/H_{1,1} = 0.68$  and  $H_{3,3}/H_{1,1} = 3.5$ ,  $H_{3,2}/H_{1,2} = 2.7$ ,  $H_{1,3}/H_{1,2} = 1.03$ , which is similar to the Taylor microscale ratios for horizontal velocity terms, but with much more anisotropy in the vertical velocity terms. In HIT,  $C_{uu}(\delta y)$  goes negative at moderate separation and integral correlation lengths satisfy  $\Lambda_{1,2}/\Lambda_{1,1} = 1/2$ , but in RTI flow,  $C_{uu}(\delta x)$  goes negative instead and we find  $\Lambda_{1,2}/\Lambda_{1,1} \approx 1$ .

## D. Structure functions

Since the classical work of Kolmogorov in 1941<sup>13</sup>, structure functions have been used extensively to characterize turbulence in the inertial range<sup>14</sup>. The second-order structure function is directly related to the scaling of the energy spectrum<sup>15,16</sup>, while straining and sweeping motions<sup>12,17</sup> can be analyzed theoretically and experimentally in terms of higher order structure functions<sup>18–20</sup>. Structure functions of order  $n$  for variable  $a$  are given by

$$S^{(n)}(\mathbf{r}) = \langle [a(\mathbf{x} + \mathbf{r}) - a(\mathbf{x})]^n \rangle, \quad (19)$$

which are related to the autocorrelation functions in the previous section for  $n = 2$ . The Batchelor parametrization of the 2nd order structure function is given by<sup>16</sup>

$$S_B^{(2)}(r) = (\langle \varepsilon \rangle / 3\nu) r^2 [1 + (1/3B)^{3/2} (r/\eta)^2]^{-2/3}, \quad (20)$$

where  $B$  is a constant. It is not clear how to generalize this to anisotropic flow, nor even to longitudinal and transverse directions. For correlations and structure functions computed in homogeneous regions, one has the relation  $S^{(2)} = 2\langle u_\alpha^2 \rangle (1 - C(r))$ , where  $C$  is the autocorrelation function for the velocity component  $u_\alpha$ . Because the radius of curvature of  $C$  at  $r = 0$  is equal to the corresponding Taylor microscale  $\lambda$ ,  $S^{(2)} \rightarrow \langle u_\alpha^2 \rangle r^2 / \lambda^2$  as  $r \rightarrow 0$ . For longitudinal structure we would expect from Eq. (13) that a suitable prefactor would be  $\langle \varepsilon \rangle / 15\nu$  in an equation of the form of (20).

In Figure 6, the transverse and longitudinal 2nd order structure functions are shown for the vertical velocity component  $w$  at the midplane for small separations. In the longitudinal (vertical) direction there is a slight asymmetry between bubble side ( $\delta z > 0$ ) and spike side ( $\delta z < 0$ ). A Batcheloresque form

$$S_B^{(2)}(r) / \langle w^2 \rangle = (r/\lambda)^2 [1 + (1/3B)^{3/2} (r/\eta)^2]^{-2/3} \quad (21)$$

is also shown in Figure 6 (dashed lines) using  $B = 7.9$  for the transverse and 11.0 for the longitudinal direction. The transverse (horizontal) structure function fits this form quite well out to  $r/\lambda = 10$ , but the longitudinal curves deviate noticeably and never even really develop a distinct  $r^{2/3}$  regime. This may be due to an insufficiently high value of  $h/\lambda$  in the simulation.

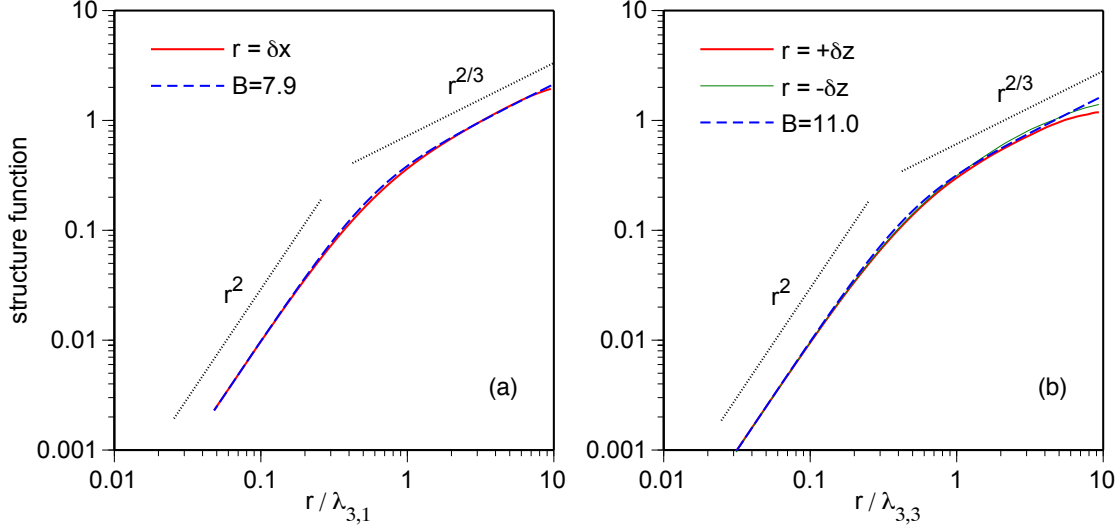


FIG. 6. (Color online) Midplane 2nd-order structure function for the vertical velocity, scaled by  $\langle w^2 \rangle$ , in the  $A = 0.5$  case at  $t = 25$  for (a) transverse separations ( $r = \delta x$ ) and (b) longitudinal separations ( $r = \pm \delta z$ ) showing  $r^2$  behavior for small separations and approximate  $r^{2/3}$  behavior for large separations. The model in (21) is shown with dashed lines using an eyeball fit for parameter  $B$ .

### E. Component energy and vorticity spectra

The component energy spectra can provide relevant information regarding the degree of anisotropy at different spatial scales, although this is limited to the extent that some representation of spectra can be constructed for the inhomogeneous flow direction. One-dimensional energy spectra for different velocity and vorticity components are shown in Figure 7. The 1D (co)spectrum in the horizontal direction  $x$  is computed with discrete Fourier transforms of functions  $\phi$  (and  $\psi$ ) in  $x$ , denoted  $\hat{\phi}$  (and  $\hat{\psi}$ ), and the power is averaged over the other horizontal direction  $y$  and optionally over different vertical positions  $z$ ,

$$E_{\phi\psi}(k_1|z) = \frac{1}{L_y L_z} \int_{-L_y/2}^{L_y/2} \int_{z-L_z/2}^{z+L_z/2} \Re \left\{ \hat{\phi}(k_1|y', z') \hat{\psi}^*(k_1|y', z') \right\} dy' dz', \quad (22)$$

and likewise for the 1D (co)spectrum in the horizontal direction  $y$ , changing  $k_1$  to  $k_2$  and  $y$  to  $x$ . We use the property for periodic functions that the correlation function and power spectrum are Fourier transforms of one another to construct approximate “pseudo-spectra” in the vertical direction  $z$ . Vertical correlation functions (cf. §III C, Figs. 5a & c) are

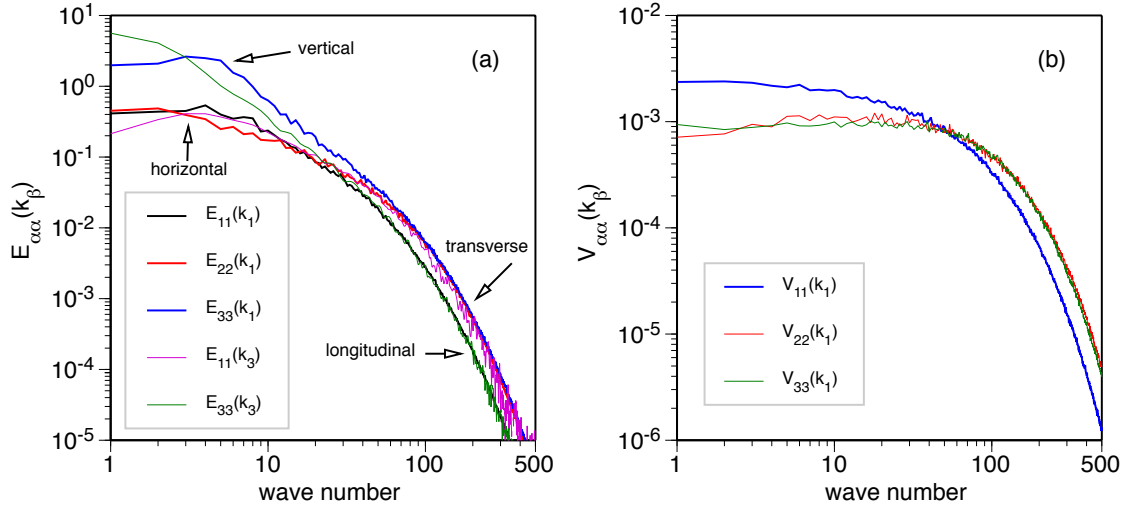


FIG. 7. (Color online) One-dimensional spectra of (a) velocity and (b) vorticity at midplane at  $t = 25$  in the  $A = 0.5$  case. Vertical spectra (in  $k_3$ ) for velocity components were constructed using Fourier transforms of vertical autocorrelation functions. Statistically equivalent terms have been averaged together.

made symmetric for positive and negative separations around midplane using the function  $[R_{\phi\psi}(\delta z|z_0) + R_{\phi\psi}(-\delta z|z_0)]/2$ , then Fourier transformed to give  $E_{\phi\psi}(k_3|z_0)$ . The 1D spectrum of a velocity component in the same direction as the velocity component,  $E_{\alpha\alpha}(k_\alpha)$ , is called a “longitudinal” spectrum, and the 1D spectrum of a velocity component in a direction perpendicular to the velocity component,  $E_{\alpha\alpha}(k_\beta)$ ,  $\alpha \neq \beta$ , is called a “transverse” spectrum. Two-dimensional horizontal (co)spectra,  $E_{\phi\psi}(k|z)$ , are computed by binning the power of 2D discrete Fourier transforms in  $x$  and  $y$  of functions  $\phi$  (and  $\psi$ ) in bands of wave number magnitude, and optionally averaging over different vertical positions  $z$ :

$$E_{\phi\psi}(k|z) = \frac{1}{L_z} \int_{z-L_z/2}^{z+L_z/2} \sum_{\kappa=k-\Delta k/2}^{\kappa=k+\Delta k/2} \Re \left\{ \hat{\phi}(k_1, k_2|z') \hat{\psi}^*(k_1, k_2|z') \right\} dz', \quad (23)$$

where  $\kappa = (k_1^2 + k_2^2)^{1/2}$ . Both 1D and 2D discrete spectral functions are normalized such that their sums over all represented wave numbers equals the mean of the product of the functions,

$$\langle \phi\psi \rangle = \sum_{k_\alpha=0}^{k_{\alpha \max}} E_{\phi\psi}(k_\alpha) \Delta k_\alpha = \sum_{k=0}^{k_{\max}} E_{\phi\psi}(k) \Delta k. \quad (24)$$

One-dimensional energy spectra in transverse directions near midplane in Figure 7a show

that the velocity fluctuations tend to become isotropic at small dissipation scales. This can also be demonstrated in longitudinal directions using the vertical pseudo-spectra. Although the vertical pseudo-spectra are noisy at high wave numbers, the results suggest that both longitudinal and transverse spectra for all velocity components collapse isotropically at small scales. In contrast, at the large spatial scales (low wave number modes) the anisotropy remains quite pronounced.

Differences in the 1D horizontal vorticity spectra (Fig. 7b) can be ascribed to different mixtures of longitudinal and transverse velocity derivative components. The  $V_{22}(k_1)$  and  $V_{33}(k_1)$  spectra are nearly equal while the  $V_{11}(k_1)$  spectrum differs with more power at low wave numbers. Spectra for the velocity derivatives in the vorticity terms group together depending on whether the spectral direction is longitudinal or transverse with respect to the underlying velocity component, and  $V_{11}(k_1)$  is comprised of two transverse terms while the others are a mix of longitudinal and transverse. Note that 2D vorticity spectra in horizontal planes (not shown) give the more expected result that  $V_{11}(k)$  and  $V_{22}(k)$  are statistically equivalent and differ from  $V_{33}(k)$ .

A generalized energy spectrum was proposed for RTI flow by Zhou<sup>21</sup> that takes into account the influences of both the external driver and turbulent nonlinear interactions<sup>22</sup>. The inertial range of this spectrum, in the form  $E(k) \sim k^{-m}$ , will exhibit a scaling exponent  $m$  that varies between the classical Kolmogorov spectrum ( $m = 5/3$ ) at higher wave numbers and one with a steeper slope ( $m = 7/4$ ) at lower wave numbers. The inertial range must be sufficiently long to exhibit this split in the RTI energy spectra. Compensated 2D horizontal spectra are shown in Figure 8 using the Kolmogorov scaling and the RTI scaling appropriate for the  $m = 7/4$  range. In one case we use only the vertical components in the energy  $E_{33}(k)$  normalized with vertical dissipation term  $\varepsilon_3$ ; and in the other case we sum over all velocity components,  $E_{ii}(k)$ , and normalize with the total dissipation rate  $\varepsilon$ . The slope of the vertical component alone is seen to be consistent with either a  $k^{-5/3}$  Kolmogorov spectrum or the  $k^{-7/4}$  spectrum proposed by Zhou for RTI flow<sup>21</sup>. However, the narrowness of the inertial range and the level of noise in the numerical simulation data unfortunately make it difficult to distinguish clearly the small difference in slopes between these two scalings or to observe the predicted change in slopes. We observe that scaling velocity terms by  $(gAh)^{1/2}$  and density terms by  $\Delta\rho$  does a fairly good job collapsing the data for different Atwood numbers, at least for the low-to-moderate density ratios considered here. Because the dissipation rate

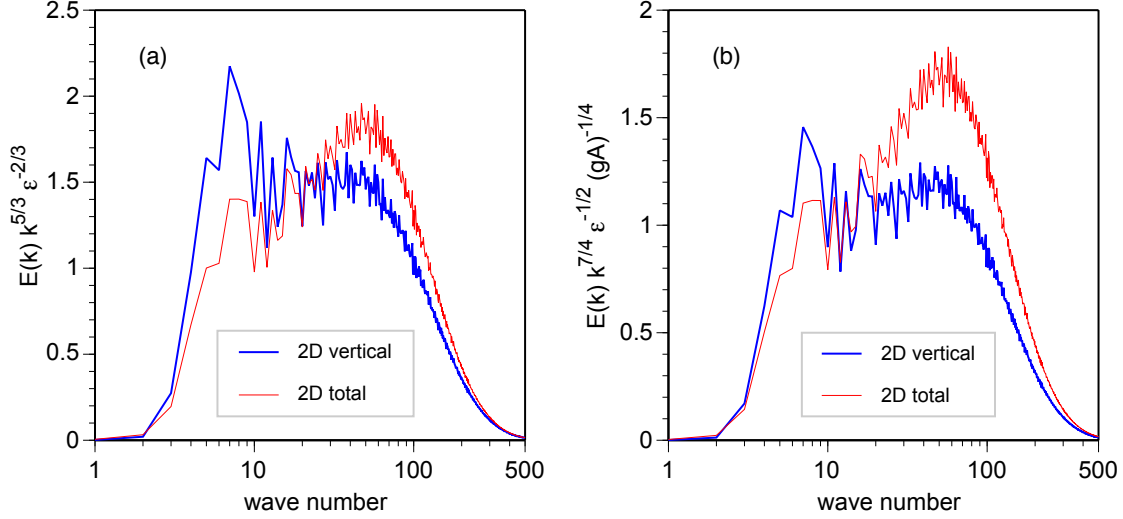


FIG. 8. (Color online) Compensated 2D horizontal spectra for the vertical velocity component  $E_{33}(k)$  (thick lines) and for the sum of all velocity components  $E_{ii}(k)$  (thin lines) calculated near the midplane at  $t = 25$  for the  $A = 0.5$  case. In (a) the  $k^{-5/3}$  Kolmogorov scaling is used, and in (b) the  $k^{-7/4}$  Rayleigh-Taylor scaling proposed by Zhou<sup>21</sup> is used.

is observed to be about 1/2 the production rate in RTI flow<sup>5</sup>, the mass-specific dissipation rate  $\epsilon \approx g_z \langle \rho w \rangle / 2 \langle \rho \rangle$  should scale as  $gA(gAh)^{1/2}$ . With these scalings, both the Kolmogorov and Zhou compensated spectra are independent of Atwood number.

Values of  $\sim 1.5$  for the plateau region of the compensated spectra in Figure 8a are consistent with results from other simulations of turbulent flows<sup>23</sup>. Note, however, Yeung & Zhou<sup>23</sup> found that at higher Reynolds numbers in HIT there will be a second relatively flat region. These authors determined that this lower wave number region, rather than the plateau itself, represents the beginning of a proper inertial range. Also, at the high-wave-number end of the inertial range of HIT, a region of shallower slope is sometimes observed (which appears as a bump in compensated spectra) and is attributed to a “bottleneck” effect in the turbulence cascade<sup>24–26</sup>. While a slight rise is seen in the compensated spectra at the high-wave-number end of the plateau regions in Figure 8, the inherent anisotropy in the spectral components, as well as the limited dynamic range of the spectra here, precludes any definitive statement about such detailed structure in RTI flow spectra at this time.

The horizontal velocity components are seen in Figure 7 to have much shallower spectra than the vertical component as a result of anisotropic forcing<sup>5</sup>. Because of this, the com-

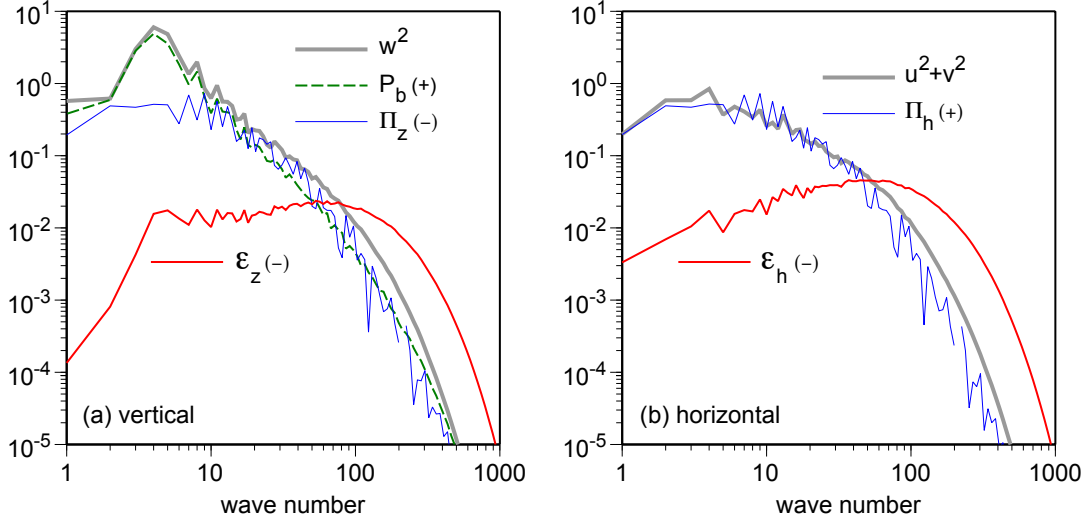


FIG. 9. (Color online) Horizontal midplane spectra for (a) vertical and (b) horizontal kinetic energy rate terms: buoyancy production (dashed line), pressure-strain (thin solid line), and dissipation (medium solid line). The pressure-strain term is a sink (-) for the vertical kinetic energy and a source (+) for the horizontal kinetic energy. The thick curves show the corresponding vertical and horizontal velocity spectra.

pensated spectra for the sum of all velocity components in Figure 8 do not fit the proposed scalings at all. The difference in forcing between vertical and horizontal velocity components is demonstrated in Figure 9, which shows the (horizontal) scale distribution of terms in the vertical and horizontal kinetic energy equations,

$$\left(\frac{1}{2}\rho w^2\right)_{,t} + \left(\frac{1}{2}\rho w^2 u_j - w\tau_{zj}\right)_{,j} = \rho w g_z - w p_{,z} - w_{,j}\tau_{zj} , \quad (25)$$

$$\left(\frac{1}{2}\rho u_i^2\right)_{,t} + \left(\frac{1}{2}\rho u_i^2 u_j - u_i\tau_{ij}\right)_{,j} = -u_i p_{,i} - u_{i,j}\tau_{ij} , \quad (26)$$

whose global averages, denoted by angle brackets, are given by

$$\left\langle \frac{1}{2}\rho w^2 \right\rangle_{,t} = +\langle \rho w \rangle g_z - \langle -p w_{,z} \rangle - \langle w_{,j}\tau_{zj} \rangle \equiv +P_b - \Pi_z - \varepsilon_z , \quad (27)$$

$$\left\langle \frac{1}{2}\rho u_i^2 \right\rangle_{,t} = +\langle p u_{i,i} \rangle - \langle u_{i,j}\tau_{ij} \rangle \equiv +\Pi_h - \varepsilon_h , \quad (28)$$

where the index  $i$  is summed over only  $x$  and  $y$  in (26) and (28). (Note that  $\varepsilon_z$  and  $\varepsilon_h$  here are volume-specific dissipation rates.) Buoyancy production, pressure-strain, and dissipation terms appear on the right-hand sides of (27) and (28) with + and - signs to indicate if they

are sources or sinks. Two-dimensional horizontal cospectra are calculated near the midplane using their constituent terms ( $g_z$  being constant in the buoyancy production term). Because the flow is nearly incompressible at late times, the pressure-strain terms nearly balance, i.e.,  $\Pi_h \approx \Pi_z$ . The vertical component is forced at the largest scales by buoyancy production ( $P_b$ ). The horizontal scales, on the other hand, have energy injected at intermediate scales via the pressure-strain ( $\Pi_h$ ) at the expense of the vertical kinetic energy ( $-\Pi_z$ ), and the dynamic range in the simulation is probably inadequate to allow the horizontal scales to achieve a Kolmogorov-like spectrum. The shape of the spectra for vertical and horizontal velocity components is overlaid on their respective production spectra in Figure 9 to highlight their close resemblance, especially at larger scales; the velocity spectra have somewhat greater small-scale energy content than the production spectra as a result of the turbulence cascade.

*Reynolds numbers and inertial range requirements.* At large enough Reynolds number a turbulent flow develops an inertial range — a well-defined power-law region at intermediate scales that separates large energy-containing scales and small dissipative scales. It is thought that turbulence at inertial range scales take on a universal character independent of the type of large-scale forcing in the flow. The existence and extent of the inertial range is often discussed in terms of the outer-scale Reynolds number based on the inertial scale  $\ell$ , which characterizes the size of energy-containing turbulent eddies (see §III B); in RTI flow,  $\ell$  is comparable to the mixing layer width  $h$ . The inertial-scale Reynolds number for HIT<sup>12</sup> is  $\text{Re}_\ell = (\ell/\eta)^{4/3} = \langle 3u_\alpha^2/2 \rangle^{1/2} \ell/\nu = 3\text{Re}_\lambda^2/20$ , where  $\eta$  is the Kolmogorov scale (15) and  $\text{Re}_\lambda$  is the Taylor-microscale Reynolds number; values of  $\text{Re}_\ell$  are comparable to those based on mixing layer width and growth rate,  $\text{Re}_h = h\dot{h}/\nu$ . To the eye, the range in high Reynolds number spectra<sup>27</sup> that appears to have power-law behavior extends from wavelengths about 5 times shorter than the peak in energy spectrum (which we associate with  $\ell$ ) to about  $50\eta$ ; this only requires  $\text{Re}_\lambda > 100$  with an overall range of about  $(\text{Re}_\lambda/100)^{3/2}$ . Dimotakis<sup>10</sup> postulated, however, that the long-wavelength end of the inertial range actually begins at the Liepmann-Taylor scale,  $\Lambda = (5/2)^{1/2}\lambda$ , giving a much narrower range of about  $\Lambda/50\eta = (\text{Re}_\ell/10^4)^{1/4} = (\text{Re}_\lambda/258)^{1/2}$ . This limiting value of  $\text{Re}_\lambda \approx 250$  is only high enough for the first appearance of the inertial range. Triadic interaction analysis provides an estimate of the desired minimum length of the inertial range<sup>11</sup> based on the scaling of local and nonlocal interactions<sup>28,29</sup>. The critical Taylor-microscale Reynolds number of the minimum state obtained from that study has a higher value of about 560. In any case, to



qualify as fully developed turbulence in these more rigorous senses, the Taylor-microscale Reynolds numbers in DNS or laboratory experiments of RTI turbulent flow should achieve values greater than  $\sim 250$  *in all directions*.

The Taylor-microscale Reynolds numbers for vertical velocity components in the DNS results are about 200–400 at the latest times (see Table III), which is marginally near the level needed to form an inertial range, but those for the horizontal components are 3–4 times lower at the sub-100 level. This disparity manifests itself in the power spectra shown in Figures 7 & 9, in which the vertical velocity component appears to be developing a well-defined  $-5/3$  power-law region, but the less energetic horizontal components do not exhibit any power-law behavior in their spectra. The commingling of energy and dissipation scales that occurs in these numerical simulations means that their spectra do not achieve a universal inertial range and may explain the lack of truly self-similar behavior that was observed in some statistical quantities<sup>5</sup>.

The results presented in this subsection strongly suggest that a single, outer-scale Reynolds number ( $Re$ ) is inadequate for characterizing highly anisotropic turbulence. The outer-scale Reynolds number  $Re \sim 10^4$ , which blends all velocity components, appears to be sufficient to achieve fully developed turbulence in the numerical simulations; but the horizontal flow components, with a Taylor-microscale Reynolds number  $Re_{\lambda 1} < 100$ , are clearly not turbulent.

## F. Skewness and Flatness

The skewness and flatness of the velocity derivatives are significant indicators of the properties of turbulent flows. In HIT, the skewness of the velocity derivatives indicates the rate of production of vorticity through vortex stretching<sup>30</sup>. Indeed, the non-zero value arises from the nonlinearity of the Navier-Stokes equations, and the classical Kolmogorov theory predicts a value independent of Reynolds number<sup>15,31</sup>. The flatness of velocity derivatives, on the other hand, provides a way to assess the intermittency of the inertial range<sup>32</sup>. However, these factors have not been measured previously in high Reynolds number RTI turbulence. The skewness  $S$  and flatness  $F$  are given by

$$S = \langle u_{\alpha,\beta}^3 \rangle / \langle u_{\alpha,\beta}^2 \rangle^{3/2}, \quad F = \langle u_{\alpha,\beta}^4 \rangle / \langle u_{\alpha,\beta}^2 \rangle^2. \quad (29)$$

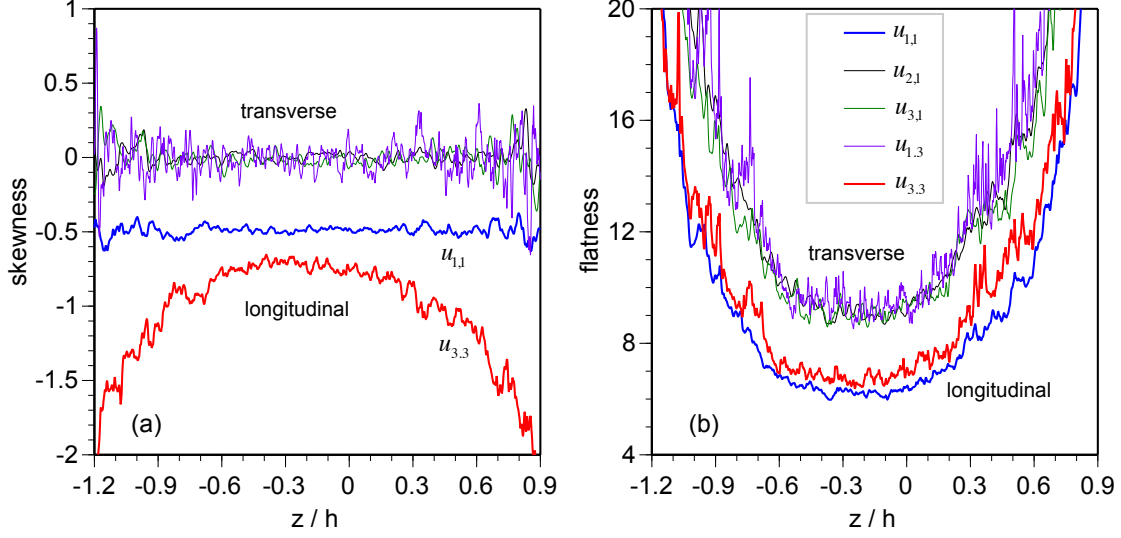


FIG. 10. (Color online) Vertical profiles of (a) skewness and (b) flatness for velocity derivatives at  $t = 25$  for the  $A = 0.5$  case.

These are plotted in Figure 10 at midplane with a horizontal plane average. The skewness for transverse derivatives is noisy but appears to be zero on average, and it is finite for longitudinal derivatives. The skewness for horizontal longitudinal derivatives is about  $-0.5$  across most of the mixing layer (deviating only at the outer edges), while the skewness for the vertical longitudinal derivative ( $u_{3,3}$ ) varies across the mixing layer with a value of about  $-0.7$  in the middle and progressively more negative values toward the outer regions. The flatness also varies a great deal across the mixing layer, with minimum values at near midplane of about  $6.5$  for longitudinal derivatives and  $9.0$  for transverse derivatives. Values of flatness greater than the gaussian value of  $3$  indicate the presence of intermittency.

These values are in good agreement with the experimental measurements<sup>31–33</sup>, in which the skewness and flatness of the longitudinal velocity derivative were found to be around  $-0.5$  to  $-0.6$  and  $6$  to  $7$ , respectively, at comparable values of the Taylor microscale Reynolds number. Jiménez et al.<sup>34</sup> studied these measurements in HIT using DNS. At Taylor microscale Reynolds number of  $168$ , the skewness and flatness of the velocity derivative for  $u_{1,1}$  were found to be  $-0.525$  and  $6.1$ , respectively. The flatness of the transverse gradients  $u_{1,2}$  was found to be  $9.4$ . In DNS of RTI flow with lower Reynolds number and small Atwood number, values of vertical and horizontal longitudinal skewness of  $-1.0$  and  $-0.2$  were observed<sup>35</sup>, and in simulations of buoyancy-driven variable-density turbulence, values of around  $-0.7$  and  $-0.4$

were observed<sup>36</sup>. While these results are in general agreement with previous experimental and simulation measurements, note that the values of the velocity-derivative flatness should increase as  $Re_\lambda$  increases with time in the RTI-driven flow. The larger values seen here toward the edges of the mixing region likely arise from lack of self-similarity there rather than Reynolds number effects<sup>35</sup>.

## G. Strain rate eigenvalues

The character of the turbulence in the mixing layer is essentially the same at all Atwood numbers and is typical of any fully turbulent flow. The three real eigenvalues of the velocity strain tensor  $\mathbf{S}$  and their associated eigenvectors were calculated in the midplane region at late times. There is a positive (extensional) eigenvalue  $\sigma_1$ , an intermediate eigenvalue  $\sigma_2$  of either sign, and a negative (compressive) eigenvalue  $\sigma_3$ ; their sum is the dilatation (divergence of velocity), which is negligibly small in well-developed, turbulent RTI flow. The ratios of these eigenvalues ( $\sigma_1:\sigma_2:\sigma_3$ ) is on average about 4:1:-5, which is close to the values of 3:1:-4 found in many types of turbulent flows<sup>37</sup>.

Vortex stretching is the mechanism by which energy is transferred to smaller scales in turbulent flow, and understanding the alignment of vorticity and strain in turbulence may aid in developing and evaluating subgrid-scale models<sup>38</sup>. The production term for enstrophy  $\|\boldsymbol{\omega}\|^2$  is  $P_\omega = \boldsymbol{\omega} \cdot \mathbf{S} \cdot \boldsymbol{\omega}$ , where  $\boldsymbol{\omega}$  is the vorticity pseudovector, and the corresponding production term for  $\|\nabla\rho\|^2$  is proportional to  $P_{\nabla\rho} = -\nabla\rho \cdot \mathbf{S} \cdot \nabla\rho$ . The strain tensor can be written in dyadic notation in terms of unit eigenvectors  $\mathbf{e}_i$  as

$$\mathbf{S} = \sum_{i=1}^3 \mathbf{e}_i \sigma_i \mathbf{e}_i, \quad (30)$$

hence

$$P_\omega = \sum_{i=1}^3 (P_\omega)_i = \|\boldsymbol{\omega}\|^2 \sum_{i=1}^3 \sigma_i \cos^2(\mathbf{e}_i, \boldsymbol{\omega}) \quad (31)$$

and

$$P_{\nabla\rho} = \sum_{i=1}^3 (P_{\nabla\rho})_i = -\|\nabla\rho\|^2 \sum_{i=1}^3 \sigma_i \cos^2(\mathbf{e}_i, \nabla\rho), \quad (32)$$

where  $\cos(\mathbf{a}, \mathbf{b}) = \mathbf{a} \cdot \mathbf{b} / (\|\mathbf{a}\| \|\mathbf{b}\|)$  is the cosine of the angle between the vectors  $\mathbf{a}$  and  $\mathbf{b}$ .

A histogram of the cosine of the angles is shown in Figure 11, and mean values of the square of the cosines are tabulated in Table IV for the middle of the mixing layer at late

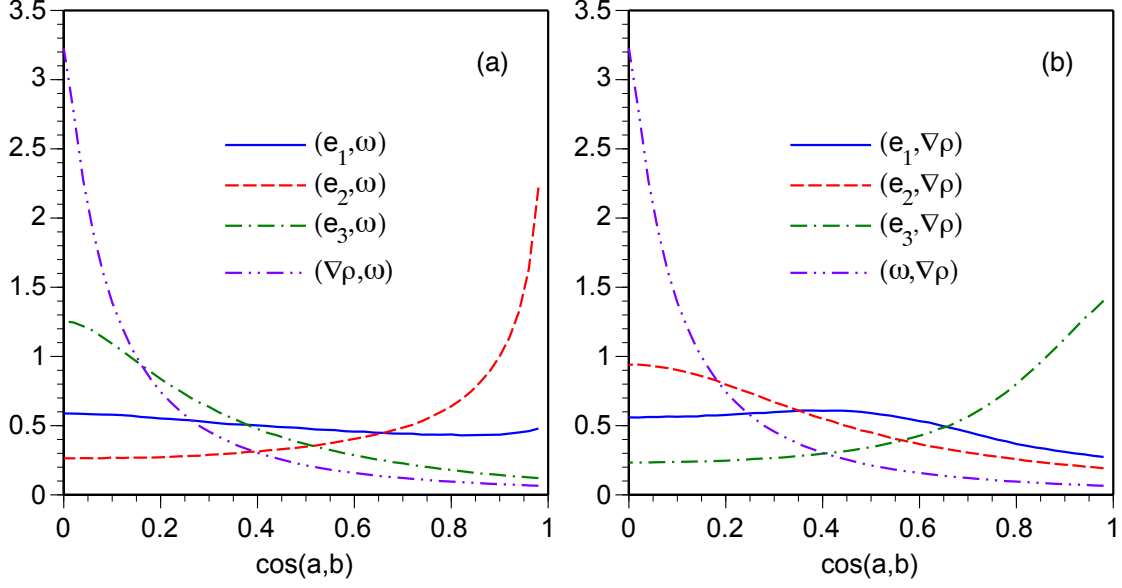


FIG. 11. (Color online) Histograms of the cosine of angles between strain rate eigenvectors, vorticity, and density gradient in the middle of the mixing layer at  $t = 25$  in the  $A = 0.5$  case. Values near unity correspond to parallel alignment of the vectors, and values near zero correspond to orthogonal alignment.

TABLE IV. Mean properties of strain rate eigenvalues, vorticity, and density gradient in the middle of the mixing layer at late time in the simulations for different Atwood numbers.

Atwood number	0.2	0.5	0.8
$\langle \sigma_3 / \sigma_1 \rangle$	-1.23	-1.23	-1.23
fraction of $\sigma_2 > 0$	0.76	0.76	0.76
$\langle \cos^2(\mathbf{e}_1, \boldsymbol{\omega}) \rangle$	0.31	0.31	0.30
$\langle \cos^2(\mathbf{e}_2, \boldsymbol{\omega}) \rangle$	0.53	0.53	0.54
$\langle (P_\omega)_2 \rangle / \langle (P_\omega)_1 \rangle$	0.84	0.93	0.94
$\langle (P_\omega)_3 \rangle / \langle (P_\omega)_1 \rangle$	-0.49	-0.49	-0.50
$\langle \cos^2(\mathbf{e}_1, \nabla \rho) \rangle$	0.27	0.28	0.28
$\langle \cos^2(\mathbf{e}_3, \nabla \rho) \rangle$	0.53	0.52	0.52
$\langle (P_{\nabla \rho})_2 \rangle / \langle (P_{\nabla \rho})_1 \rangle$	0.10	0.09	0.07
$\langle (P_{\nabla \rho})_1 \rangle / \langle (P_{\nabla \rho})_3 \rangle$	-0.23	-0.25	-0.30
$\langle \cos^2(\boldsymbol{\omega}, \nabla \rho) \rangle$	0.09	0.09	0.09

time, providing measures of the correlation between strain eigenvectors, vorticity, and density gradient. The vorticity tends to align best with the eigenvector of the middle eigenvalue  $\sigma_2$  and to a much lesser extent with the eigenvector of the most positive eigenvalue  $\sigma_1$ , but the positive and middle eigenvalue contribute comparable amounts to enstrophy production because  $\sigma_1$  is considerably larger than  $\sigma_2$ , giving a production ratio of about 2:2:-1. We observe that the density gradient aligns best with the eigenvector for the compressive eigenvalue  $\sigma_3$ , again consistent with other turbulent flows<sup>37,39</sup>. The difference in sign of the production of density gradient means that only the compressive term enhances density gradients. The production ratio for density gradients is about -1:0:3 to -1:0:4. Consistent with these results, we find that the correlation between density gradient and vorticity is very low, with average values of  $\cos^2(\boldsymbol{\omega}, \nabla\rho) \approx 0.09$ , indicating that the density gradient tends to align orthogonal to the vorticity<sup>40</sup>. Note that there is very little sensitivity to the Atwood number in these results.

#### IV. CONCLUSIONS

In this work, we have provided some detailed statistics measurements that are important for improving our understanding the physics of turbulent flow induced by Rayleigh-Taylor instability. Direct numerical simulation data for miscible fluids with unity Schmidt number and moderate density contrasts (3/2 to 9) were used for this study. Specifically, we have examined the degree to which the anisotropy generated by the gravity impacts the length scales, correlation functions, structure functions, spectra, skewness and flatness. We have also investigated the alignment of eigenvectors of the strain rate, density gradient, and vorticity. In general, the large turbulent scales are highly anisotropic due to buoyancy forces in the direction of gravity, but the flow becomes much more isotropic at small scales in the core of the mixing layer. As a result, the velocity displays a high degree of anisotropy while its derivatives behave much more isotropically. Many statistical quantities derived from velocity derivatives in the middle of the mixing layer have similar properties to those in homogenous, isotropic turbulence, lending support to the notion of universal small-scale structure in turbulent flows, regardless of whether they are forced isotropically or anisotropically at large scales. The turbulence statistics are found to be insensitive to the density contrast in the range of values considered here.

It is important to stress the disparate Taylor-microscale Reynolds numbers in the vertical and horizontal components of the velocity field in the numerical simulation results examined here; the vertical measure appears to qualify as marginally turbulent while the horizontal measure falls short. The vertical velocity components are forced predominantly at long wavelengths by buoyancy and exhibit a nascent inertial range as energy cascades to smaller scales; the horizontal velocity components, on the other hand, are forced by pressure-strain terms at somewhat shorter wavelengths and do not exhibit anything like a Kolmogorov spectrum. This observation suggests that the behavior of a number of important statistical measurements for these two components is rather distinctive and should be considered separately at these modest Reynolds numbers. Direct numerical simulations of RTI flow that qualify as fully turbulent with a universal inertial range will require Taylor-microscale Reynolds numbers to be greater than  $\sim 250$  *in all directions* and will therefore need to use much greater computational resources than those considered here.

## ACKNOWLEDGMENTS

This work was performed under the auspices of the Lawrence Livermore National Security, LLC under contract No. DE-AC52-07NA27344.

## REFERENCES

- <sup>1</sup>Lord Rayleigh, “Investigation of the character of the equilibrium of an incompressible heavy fluid of variable density,” *Proc. R. Math. Soc.* **14**, 170–177 (1883).
- <sup>2</sup>G. I. Taylor, “The instability of liquid surfaces when accelerated in a direction perpendicular to their plane,” *Proc. R. Soc. London A* **201**, 192–196 (1950).
- <sup>3</sup>A. W. Cook, W. H. Cabot, and P. L. Miller, “The mixing transition in Rayleigh-Taylor instability,” *J. Fluid Mech.* **511**, 333–362 (2004).
- <sup>4</sup>Y. Jang and S. M. de Bruyn Kops, “Pseudo-spectral numerical simulation of miscible fluids with a high density ratio,” *Computers & Fluids* **36**, 238–247 (2007).
- <sup>5</sup>W. H. Cabot and A. W. Cook, “Reynolds number effects on Rayleigh-Taylor instability with possible implications for type-1a supernovae,” *Nature Physics* **2**, 562–568 (2006).

- <sup>6</sup>W. Cabot, “Comparison of two- and three-dimensional simulations of miscible Rayleigh-Taylor instability,” *Phys. Fluids* **18**, 045101 (2006).
- <sup>7</sup>C. A. Kennedy, M. H. Carpenter, and R. M. Lewis, “Low-storage, explicit Runge-Kutta schemes for the compressible Navier-Stokes equations,” *Applied Numerical Math.* **35** 177–219 (2000).
- <sup>8</sup>R. A. Antonia and J. Kim, “A numerical study of local isotropy of turbulence,” *Phys. Fluids* **6**, 834–841 (1994).
- <sup>9</sup>J. O. Hinze, *Turbulence* (McGraw-Hill, 1959).
- <sup>10</sup>P. E. Dimotakis, “The mixing transition in turbulence,” *J. Fluid Mech.* **409**, 69–97 (2000).
- <sup>11</sup>Y. Zhou, “Unification and extension of the similarity scaling criterion and mixing transition for studying astrophysics using high energy density laboratory experiments or numerical simulations,” *Phys. Plasma* **14**, 082701 (2007).
- <sup>12</sup>H. Tennekes and J. L. Lumley, *A First Course in Turbulence* (MIT Press, 1972).
- <sup>13</sup>A. N. Kolmogorov, “The local structure of turbulence in incompressible viscous fluid for very large Reynolds numbers,” *Proc. Royal Society of London A* **434**, 9–13 (1991).
- <sup>14</sup>U. Frisch, *Turbulence* (Cambridge Univ. Press, 1996).
- <sup>15</sup>A. S. Monin and A. M. Yaglom, *Statistical Fluid Mechanics: Mechanics of Turbulence, Vol. 2*, (MIT Press, 1975).
- <sup>16</sup>D. Lohse and A. Müller-Groeling, “Anisotropy and scaling corrections in turbulence,” *Phys. Rev. E* **54**, 395–405 (1996).
- <sup>17</sup>Y. Zhou, “Renormalization group theory for fluid and plasma turbulence,” *Phys. Rep.* **488**, 1–49 (2010).
- <sup>18</sup>E. J. H. F. Anselmetti, Y. Gagne, and R. A. Antonia, “Higher-order velocity structure functions in turbulent shear flows,” *J. Fluid Mech.* **140**, 63–89 (1984).
- <sup>19</sup>M. Y. K. A. A. Praskovsky, E. B. Gledze, and Y. Zhou, “The sweeping decorrelation hypothesis and energy-inertial scale interaction in high Reynolds number flows,” *J. Fluid Mech.* **248**, 493–511 (1993).
- <sup>20</sup>A. Vincent and M. Meneguzzi, “The spatial structure and statistical properties of homogeneous turbulence,” *J. Fluid Mech.* **225**, 1–20 (1991).
- <sup>21</sup>Y. Zhou, “A scaling analysis of turbulent flows driven by Rayleigh-Taylor and Richtmyer-Meshkov instabilities,” *Phys. Fluids* **13**, 538–543 (2001).
- <sup>22</sup>Y. Zhou, W. H. Matthaeus, and P. Dmitruk, “Colloquium: Magnetohydrodynamic turbu-

- lence and time scales in astrophysical and space plasmas,” *Rev. Mod. Phys.* **76**, 1015–1035 (2004).
- <sup>23</sup>P. K. Yeung and Y. Zhou, “Universality of the Kolmogorov constant in numerical simulations of turbulence,” *Phys. Rev. E* **56**, 1746–1752 (1997).
- <sup>24</sup>D. Lohse and A. Müller-Groeling, “Bottleneck effects in turbulence: Scaling phenomena in  $r$  versus  $p$  space,” *Phys. Rev. Lett.* **74**, 1747–1750 (1995).
- <sup>25</sup>G. Falkovich, “Bottleneck phenomenon in developed turbulence,” *Phys. Fluids* **6**, 1411–1414 (1994).
- <sup>26</sup>Y. Kaneda, T. Ishihara, M. Yokokawa, K. Itakura, and A. Uno, “Energy dissipation rate and energy spectrum in high resolution direct numerical simulations of turbulence in a periodic box,” *Phys. Fluids* **15**, L21–L24 (2003).
- <sup>27</sup>S. G. Saddoughi and S. V. Veeravalli, “Local isotropy in turbulent boundary layers at high Reynolds number,” *J. Fluid Mech.* **268**, 333–372 (1994).
- <sup>28</sup>Y. Zhou, “Degrees of locality of energy transfer in inertial range,” *Phys. Fluids A* **5**, 1092–1095 (1993).
- <sup>29</sup>Y. Zhou, “Interacting scales and energy transfer in isotropic turbulence,” *Phys. Fluids A* **5**, 2511–2524 (1993).
- <sup>30</sup>G. I. Taylor, “Production and dissipation of vorticity in a turbulent fluid,” *Proc. R. Soc. London A* **164**, 15–23 (1938).
- <sup>31</sup>P. Burattini, P. Lavole, and R. A. Antonia, “Velocity derivative skewness in isotropic turbulence and its measurement with hot wires,” *Exp. Fluids* **45**, 523–535 (2008).
- <sup>32</sup>K. R. Sreenivasan and R. A. Antonia, “The phenomenology of small-scale turbulence,” *Annu. Rev. Fluid Mech.* **29**, 435–472 (1997).
- <sup>33</sup>C. W. Van Atta and R. A. Antonia, “Reynolds number dependence of skewness and flatness factors of turbulent velocity derivatives,” *Phys. Fluids* **23**, 252–257 (1980).
- <sup>34</sup>J. Jiménez, A. A. Wray, P. G. Saffman, and R. S. Rogallo, “The structure of intense vorticity in isotropic turbulence,” *J. Fluid Mech.* **255**, 65–90 (1993).
- <sup>35</sup>J. R. Ristorcelli and T. T. Clark, “Rayleigh-Taylor turbulence: self-similar analysis and direct numerical simulations,” *J. Fluid Mech.* **507**, 213–253 (2004).
- <sup>36</sup>D. Livescu and J. R. Ristorcelli, “Buoyancy-driven variable-density turbulence,” *J. Fluid Mech.* **591**, 43–71 (2007).
- <sup>37</sup>W. T. Ashurst, A. R. Kerstein, R. M. Kerr, and C. H. Gibson, “Alignment of vorticity



- and scalar gradient with strain rate in simulated Navier-Stokes turbulence,” *Phys. Fluids* **30**, 2343–2353 (1987).
- <sup>38</sup>B. Kosović, D. I. Pullin, and R. Samtaney, “Subgrid modeling for large-eddy simulations of compressible turbulence,” *Phys. Fluids* **14**, 1511–1522 (2002).
- <sup>39</sup>D. Livescu and J. R. Ristorcelli, “Mixing asymmetry in variable density turbulence,” in *Advances in Turbulence XII*, Vol. 132, edited by B. Eckhardt (Springer-Verlag, Berlin, 2009), pp. 545–548.
- <sup>40</sup>S. Kida and S. A. Orszag, “Enstrophy budget in decaying compressible turbulence,” *J. Scientific Comput.* **5**, 1–34 (1990).